Macromolecular Bioscience
www.mbs-journal.de

Microfluidic Synthesis of Block Copolymer Micelles: Application as Drug Nanocarriers and as Photothermal Transductors When Loading Pd Nanosheets

Miriam Abad, Gracia Mendoza, Laura Usón, Manuel Arruebo, Milagros Piñol, Víctor Sebastián, and Luis Oriol**

The synthesis of polymeric nanoparticles from a block copolymer based on poly(ethylene glycol) and a polymethacrylate containing the nucleobase analog 2,6-diacylaminopyridine is optimized by microfluidics to obtain homogeneous spherical micelles. Loading and delivery properties are studied using naproxen as a model. The incorporation of a Pd precursor in the polymer organic solution fed into the micromixer allows the preparation of Pd(II) precursor-polymer hybrid systems and the subsequent reduction with CO leads to the in situ synthesis of Pd nanosheets inside of the hydrophobic core of the polymeric micelles. This methodology is highly efficient to yield all polymeric nanoparticles loaded with Pd nanosheets as detected by electron microscopy and energy-dispersive X-ray spectroscopy. The cell viability of these Pd nanosheets-containing polymeric nanoparticles is evaluated using five cell lines, showing a high cytocompatibility at the tested concentrations without detrimental effects in cell membrane and nuclei. Furthermore, the use of these hybrid polymeric nanoparticles as photothermal transductors is evaluated using near infrared as irradiation source as well as its application in photothermal therapy using different cell lines demonstrating a high efficiency in all cell cultures.

1. Introduction

Among the different facets of polymer chemistry as a toolbox of interest in nanoscience, the self-assembly of macromolecules resulting from the chemical covalent bonding of immiscible polymeric blocks is especially appealing.[1] The phase segregation of the different segments constituting block copolymers (BCs) into a variety of periodic nanostructures has been widely used in the preparation of nanomaterials. Of particular interest are the polymeric self-assemblies of amphiphilic BCs in aqueous solutions due to their application as nanomaterials of utility in different biomedical fields. Specifically, the use of polymeric micelles in drug delivery shows several advantages in comparison to other nanocarriers such as improved stability and their ability to solubilize hydrophobic drugs into their cores, which improves hydrophobic drugs bioavailability. Other advantages of these polymeric nanoparticles (NPs) are their high stability in diluted media, consequence of low critical aggregation concentration (CAC) values, their small size, and their prolonged circulation lifetime in the bloodstream. In addition, amphiphilic BCs can be easily functionalized to respond to external stimuli and to achieve active targeting or labeling.[2,3] Following these criteria, smart polymeric nanocarriers have been described having response to a panoply of stimuli such as temperature, pH, enzymes, redox conditions, and electromagnetic fields. Among them, light is of interest because it can be externally applied when and where it is required. Photochemical

M. Abad, L. Usón, M. Arruebo, M. Piñol, V. Sebastián, L. Oriol
Instituto de Nanociencia y Materiales de Aragón (INMA)
CSIC-Universidad de Zaragoza
Zaragoza 50009, Spain
E-mail: victorse@unizar.es; loriol@unizar.es

The ORCID identification number(s) for the author(s) of this article can be found under https://doi.org/10.1002/mabi.202100528

DOI: 10.1002/mabi.202100528

M. Abad, M. Piñol, L. Oriol
Departamento de Química Orgánica
Facultad de Ciencias
Universidad de Zaragoza
Pedro Cerbuna, 12, Zaragoza 50009, Spain

G. Mendoza, L. Usón, M. Arruebo, V. Sebastián
Department of Chemical Engineering and Environmental Technologies
University of Zaragoza
Zaragoza 50018, Spain

G. Mendoza, L. Usón, M. Arruebo, V. Sebastián
Networking Research Centre on Bioengineering
Biomaterials and Nanobiomedicine (CIBER-BNN)
Madrid 28029, Spain

G. Mendoza, M. Arruebo, V. Sebastián
Aragón Health Research Institute (ISS Aragón)
Zaragoza 50009, Spain

processes in organic chromophores, which are commonly used to induce the response to light in macromolecules, are generally based on photoisomerization, photocleavage, photocrosslinking, or photoinduced rearrangement reactions promoted by UV or visible light.[4] However, biomedical applications require of wavelengths with a higher penetration depth in biological tissues, as well as having low light-induced biological damage, which is usually achievable in the near infrared (NIR) window of about 650–900 nm. Direct photochemical processes are scarcely achieved in this region using conventional organic chromophores. Two-photon processes with photosensitive organic groups, such as coumarin derivatives, can be triggered with NIR light inducing similar chemical processes to those produced by direct absorption in the corresponding UV-visible (UV–vis) region. However, for that purpose pulsed lasers with high power densities, and small areas of irradiation, are required. Upconverting NPs[5] or plasmonic metal NPs are attractive and robust alternatives in the preparation of NIR-responsive polymeric systems.

BCs have been used for the preparation of metal-polymer hybrid materials by means of a controlled preparation of metal NPs into BC assemblies either in bulk or using self-assemblies of amphiphilic BC in selective solvents as was initially reviewed by Förster and Antonietti.[6] Thus, micelles of polystyrene-*b*-poly(vinylpyridine) were used by Antonietti et al.,[7] and Möller and co-workers[8] for the successful synthesis of Au NPs inside the micelle cores previously charged with a metal salt precursor. In the case of similar Pd-polymeric hybrid materials, the stabilization of Pd NPs has been subject of intense research, as was envisaged in the pioneering work of Antonnieti et al.,[7] for their application in organic synthesis as catalysts for C–C bond formation reactions in environmentally benign experimental conditions.[9]

The tunable surface plasmon resonance and photothermal effects of metal nanomaterials, and in particular Au-based nanomaterials, are of high interest in nanobiomedical applications such as photothermal therapy using NIR as irradiation source, the combination of photothermal response with temperature-induced drug delivery (chemophotothermal therapy), or the combination of photodynamic-photothermal effects.[10] Polymers can also be employed in the design of biomedical nanoplatforms based on metal nanomaterials, mostly Au nanomaterial, previously prepared and subsequently coated with polymeric shells.[11] Alternatively, the in situ preparation of Au nanoparticles inside of polymeric nanoparticles of poly(D,L-lactic-*co*-glycolic acid) (PLGA) has been also described by our group.[12] Additionally, other noble metal NPs including Ag and Pt have also been widely studied for therapeutic applications.[13] However, the biomedical applications of Pd nanostructures were not exploited until very recently.[14] The pioneering work of Zheng and co-workers[15] demonstrated that Pd hexagonal nanosheets, obtained by a carbon monoxide-confined growth method assisted by ammonium bromide surfactants, have tunable NIR surface plasmon resonance features of application in photothermal therapy having the advantage of a higher photothermal stability in comparison to Au or Ag. Although the 2D ultrathin nature of these Pd nanosheets hinders an efficient response, a silica coating significantly improves their efficacy as photothermal agents[16] and provides synergistic chemophotothermal properties by loading drugs onto the mesoporous silica coating.[17,18] The same group has also described the preparation of ultrasmall Pd nanosheets with high photothermal yield and optimal clearance from the body and also again having the ability of coordinating chemotherapeutic agents to combine photothermal and chemotherapies.[19,20] These Pd nanosheets have also been described for their application in photoacoustic imaging[20,21] and cancer treatment by combining their photothermal properties with immunotherapy.[22]

Very recently, we have described the in situ controlled assembly of Pd nanosheets inside of exosomes derived from cancer cells for targeted bioorthogonal catalysis.[23] The procedure is conducted under mild conditions using carbon monoxide (CO) gas as reducing and growth-directing agent to promote the efficient assembly of Pd nanosheets from a Pd precursor encapsulated inside of the exosomes, and without disrupting their membrane structure.[24] Besides, the generated Pd nanosheets can be used for biomedical applications, as they have been synthesized without the use of highly toxic ammonium bromide surfactants, preserving their NIR properties.[23–25] However, the in situ preparation of Pd nanosheets inside of block polymer NPs has not been described so far.

The assembly of polymers at the nanometer scale is usually performed in conventional batch-type reactors. This type of reactors is not proper to run fast kinetic reactions, since the mixing and heat transfer are not well suited to reactions occurring in the time frame of seconds and milliseconds. Consequently, there is a limited batch-to-batch reproducibility and controllability in terms of size or cargo loading. This phenomenon is even more serious when the production volume is scaled-up, because the mixing and heat transfer efficiencies inversely increase as the reactor volume does.[26] As a result, there is often a tradeoff to maintain the ability to control the nanoscale dimension and a feasible production throughput. After more than 30 years, microfluidics has become a mature technology to face the shortcomings related to fluid manipulation. In this particular case, the small channel dimensions lead to large surface-to-volume ratios, which enhance the heat and mass transport, and then a precise control of fast kinetic reactions. In addition, a parallelization process can easily tune the production throughput. Our group has considered a large variety of available microfluidic systems where mixing and flow conditions can be tuned on demand by complex fluid dynamic designs. However, it is important to consider that the aim is to translate the production of polymeric vectors from lab to market and simple systems should be used to ease their operation by nonskilled users. As a result, interdigital micromixers were demonstrated to achieve an excellent control[12,27,28] in nanovector specifications while maintaining a production rate as high as 10 g h^{-1}.

In this work, microfluidics is applied to the preparation of polymeric NPs derived from an amphiphilic BC (**PEG-*b*-PDAP**) consisting of a poly(ethylene glycol) block and a polymethacrylate with 2,6-diacylaminopyridine (**DAP**) pendant moieties as nucleobase-analogs, which confer good self-assembly properties.[29,30] This technology is fast, scalable, and reproducible in comparison to other conventional techniques.[31–33] The application to drug delivery nanocarriers was validated using naproxen as model. In an attempt to provide NIR response to the polymeric NPs prepared by microfluidics herein, we describe the fast and efficient preparation of Pd nanosheets inside of the core of polymeric micelles without disrupting the amphiphilic BC assembly and without the need of using highly toxic surfactants.

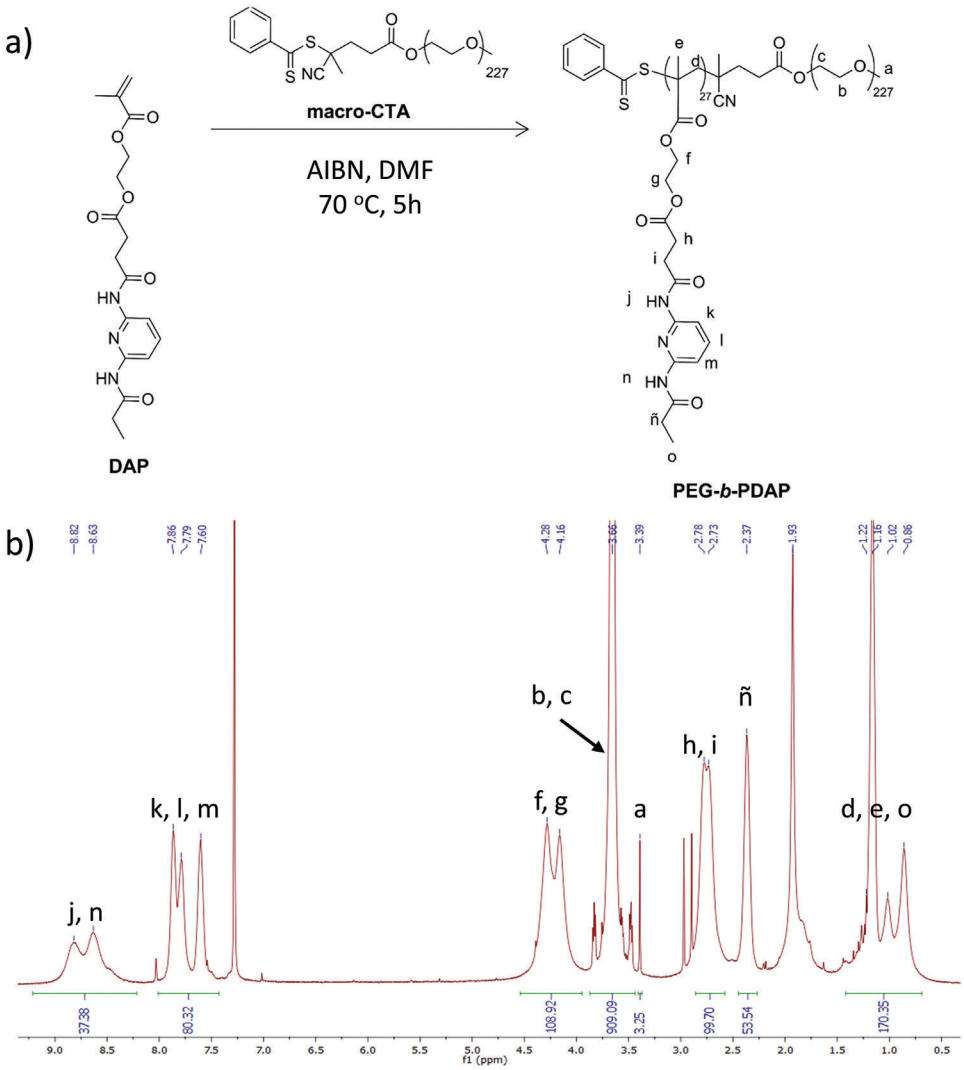

Figure 1. a) Synthesis of **PEG-*b*-PDAP** by RAFT polymerization of monomer **DAP**. b) **PEG-*b*-PDAP** ^{1}H NMR spectrum ($CDCl_3$, 400 MHz) δ (ppm).

The NIR-response of these hybrid Pd-polymeric NPs and their application in photothermal therapy using different cell lines are also studied.

2. Results and Discussion

2.1. Synthesis and Characterization of PEG-*b*-PDAP

PEG-*b*-PDAP was synthesized by reversible addition fragmentation chain transfer (RAFT) polymerization (**Figure 1**a) of the methacrylic monomer **DAP** [34] using commercially available poly(ethylene glycol) methyl ether 4-cyano-4-(phenylcarbonothioylthio)pentanoate as macromolecular chain transfer agent (**PEG-macroCTA**) with an average molar mass (M_n) of ≈10 000 g mol^{-1} (see the Experimental Section and Figure S1, Supporting Information) as previously reported.[29] The polymerization degree of the hydrophobic block and M_n of the BC were determined by ^{1}H NMR spectroscopy (Figure 1b). Comparing the relative integrations of proton signals at δ 3.43–3.89 ppm corresponding to PEG block (protons b and c) and the ones at δ 3.97–4.55 ppm corresponding to the **DAP** repeating unit (protons f and g), a degree of polymerization of 27 was estimated for the hydrophobic block when considering a polymerization degree equal to 227 for **PEG-macroCTA**. Accordingly, the average M_n was 20 480 g mol^{-1} and the estimated PEG/polymethacrylate block weight ratio was around 1:1. The dispersity ($Đ$) of the BC was 1.04 as determined by gel permeation chromatography (GPC) (Figure S2, Supporting Information) that is in agreement with values expected for a controlled radical polymerization.

2.2. Self-Assembly on PEG-b-PDAP by Nanoprecipitation in Water

Polymeric aggregates of **PEG-*b*-PDAP** were first prepared by nanoprecipitation to check self-assembly ability, by gradually adding water to a tetrahydrofuran (THF) solution of **PEG-*b*-PDAP** while monitoring changes on the light transmittance since these changes are related to self-assemblies formation (Figure S3, Sup-

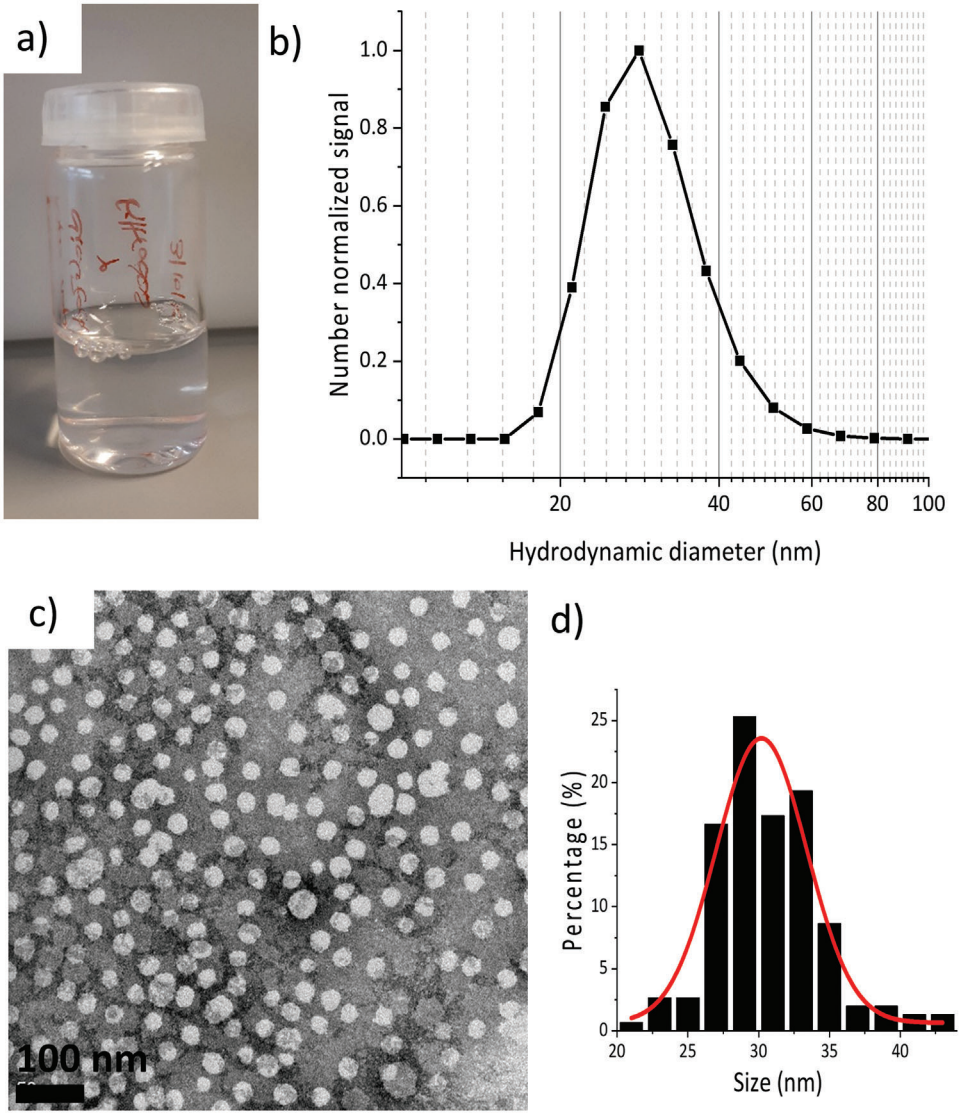

Figure 2. a) **PEG-*b*-PDAP** NPs dispersion prepared by cosolvent nanoprecipitation. b) Number particle size distribution recorded by DLS of **PEG-*b*-PDAP** NPs prepared by cosolvent nanoprecipitation. c) TEM image and d) histogram of TEM size distribution of **PEG-*b*-PDAP** NPs prepared by cosolvent nanoprecipitation.

porting Information).[35] When turbidity reached a stable value, the suspension, with a polymer concentration of 1.98 mg mL^{-1}, was dialyzed against water to obtain an aqueous dispersion of the polymeric self-assemblies (**Figure 2**a). Homogeneous spherical micelles with a diameter around 30 ± 6 nm were observed by transmission electron microscopy (TEM) (Figure 2c) that was consistent with dynamic light scattering (DLS) results, where a main distribution was observed having a hydrodynamic diameter (D_h) of 29 ± 12 nm (polydispersity index, PdI = 0.17) (Figure 2b and Figure S4, Supporting Information).

CAC of **PEG-*b*-PDAP** in water was determined by fluorescence spectroscopy using Nile Red as a fluorescent probe (Figure S5, Supporting Information).[36] **PEG-*b*-PDAP** NPs dispersions were stirred together with the Nile Red solution overnight and the emission spectra of Nile Red recorded from 560 to 700 nm while exciting at 550 nm to determine the concentration at which the fluorescence of Nile Red increases due to the micellar self- assembly and its encapsulation in the hydrophobic core. The CAC was 36 μg mL^{-1}, which is a typical value for amphiphilic BCs.[37]

2.3. Self-Assembly on PEG-b-PDAP by Microfluidics in Water

Once checked the self-assembly properties using a batch co-solvent methodology, the preparation of **PEG-*b*-PDAP** NPs was accomplished by microfluidics to check the feasibility of this methodology to produce in a continuous manner, homogeneous spherical micelles, and improve the reduced reproducibility that batch production usually suffers.

For that purpose, a solution of **PEG-*b*-PDAP** in THF was instantaneously mixed with Milli-Q water using a commercial slit interdigital microstructured mixer. Both, the polymer THF solu-

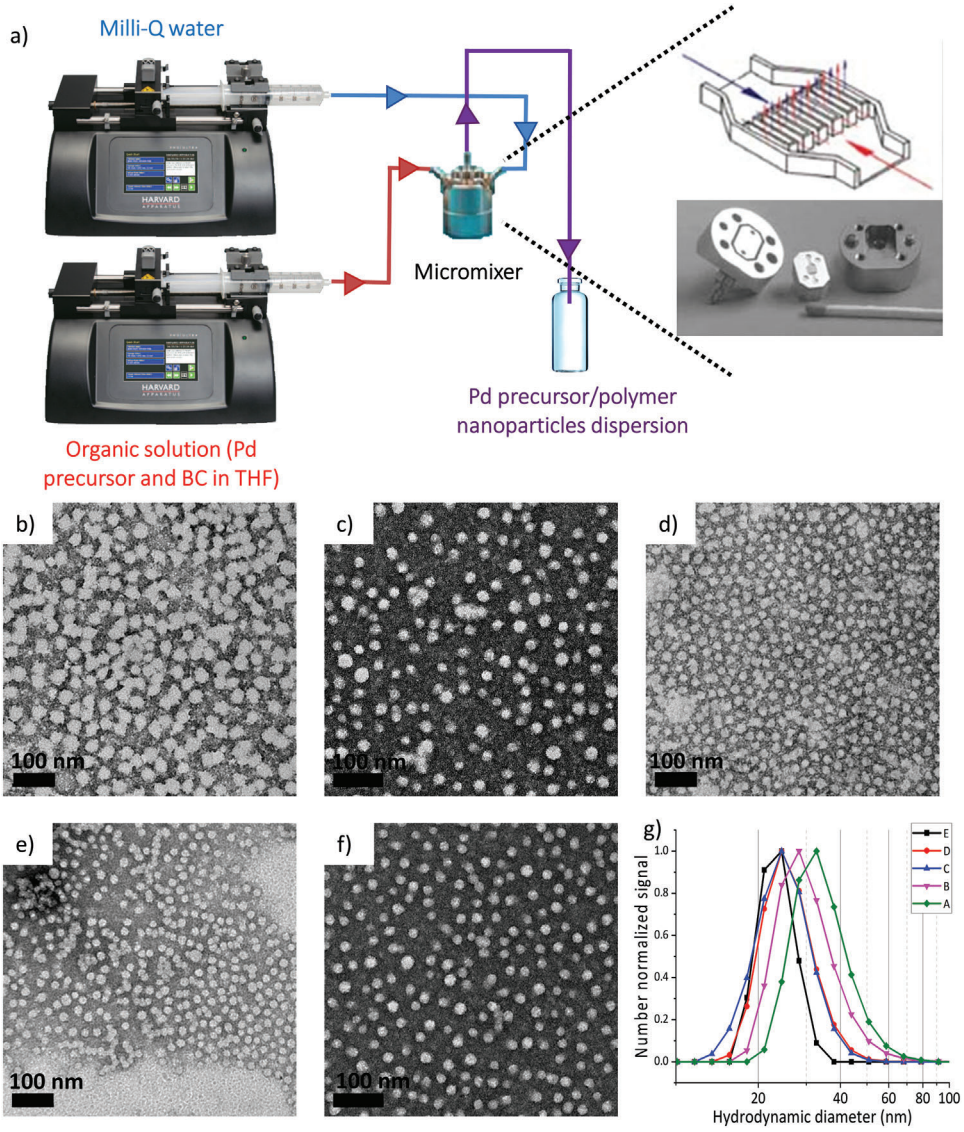

Figure 3. a) Diagram of the experimental setup for the continuous preparation of polymeric self-assemblies: Upper right inset, scheme of the flow arrangements inside the micromixer (reagents come from both sides of the central slit from where the mixed products come out); lower right inset, image of the micromixer components. TEM images of **PEG-*b*-PDAP** NPs prepared by microfluidics at 48 ms residence time (10 mL min^{-1} flow ratio) and different experimental conditions (aqueous/organic phase ratio) featured in Table 1: b) A (60:40), c) B (70:30), d) C (80:20), e) D (90:10), and f) E (95:5). g) Number particle size distributions recorded by DLS of **PEG-*b*-PDAP** NPs prepared by microfluidics at different experimental conditions (see Table 1).

tion and water were fed into the micromixer using two syringe pumps (**Figure 3**a). First, the process was optimized by checking the influence of experimental microfluidic conditions (the residence time and phase ratio values) on the self-assembly process. Four different residence times, calculated as the ratio of reactor volume/total flow rate, were tested that are 1200 ms (0.4 mL min^{-1} flow ratio), 240 ms (2 mL min^{-1} flow ratio), 48 ms (10 mL min^{-1} flow ratio), and 9.6 ms (50 mL min^{-1} flow ratio). For each residence time, two aqueous/organic solution phase ratios, 60:40 and 80:20, were evaluated according to the turbidity curve registered by nanoprecipitation (Figure S3, Supporting Information). Considering that the nanoprecipitation process is highly sensitive to the concentration profiles localized in the reaction media,[28,38] the mixing time of the organic and aqueous miscible streams should be as short as possible to promote a fast nucleation and growth of **PEG-*b*-PDAP** NPs. The slit interdigital micromixer selected to achieve a molecular mixing of reagents is able to control the efficient mixing of reagents by the shear stress generated at the fluid-fluid interphase and channel-fluid interphase.[27] This fluid mixing is achieved in a passive manner because each input flow (organic and aqueous streams) diverges into 16 slits where streams laminate into microchannels of 50 µm width, following a 90° trajectory at the mixer outlet to accelerate the mixing of reagents and promoting high shear stress (Inset Figure 3a). The best results in terms of nanoparticle size control and then efficient phases mixture were obtained for the residence

Table 1. PEG-*b*-PDAP NPs prepared by microfluidics with a residence time fixed at 48 ms (flow rate 10 mL min^{-1}): Phase ratios (aqueous solution/organic solution) conditions, final polymer concentration, D_h and PdI values determined by DLS.

Experimental conditions	Aqueous/organic solution phase ratio[a)]	Polymer concentration[b)] [mg mL^{-1}]	D_h (PdI)[c)]
A	60:40	2.00	34 ± 14 nm (0.17)
B	70:30	1.50	29 ± 12 nm (0.17)
C	80:20	1.00	25 ± 11 nm (0.19)
D	90:10	0.50	26 ± 10 nm (0.15)
E	95:5	0.25	23 ± 7 nm (0.09)

[a)] Ratio between Milli-Q water and a 5 mg mL^{-1} THF solution of **PEG-*b*-PDAP** fed into the micromixer [b)] Polymer concentration in the self-assemblies' dispersions collected at the micromixer outlet [c)] Average D_h values and PdI determined from the number particle size distribution recorded by DLS.

times of 48 and 9.6 ms. These results are in agreement with our previous work[27] where computational fluid dynamics modeling was used to elucidate and predict the best fluid dynamic conditions to promote the fast mixing in the interdigital micromixer and promote the monodisperse production of PLGA NPs. A fast flow rate induces a fast-convective mixing and high shear stress that minimize the concentration profiles of **PEG-*b*-PDAP** copolymer. Consequently, the copolymer nucleation occurs simultaneously and the growth events are similar for all NPs. Regarding the results obtained at a residence time of 48 and 9.6 ms, no remarkable differences were observed (Figure S6, Supporting Information). This fact evidences that the kinetics of the nanoprecipitation reaction is not as fast as the mixing time achieved in the micromixer and then, the nucleation/growth events for NPs produced with a residence time of 48 ms are similar than the ones at 9.6 ms. On the other hand, a residence time of 240 ms and of 1200 ms was not able to promote a mixing fast enough to compete with the nanoprecipitation kinetics and a lack of a good nanoparticle size control was observed (Figure S6c,f, Supporting Information).

Considering these facts, a residence time of 48 ms (flow rate of 10 mL min^{-1}) was selected because although the production throughput (between 1200 and 150 mg h^{-1}) was not as high as with 9.6 ms (between 6000 and 750 mg h^{-1}), the setup operability was more convenient and less waste was generated until reaching the steady state than when a residence time of 9.6 ms was selected. Therefore, once fixed the flow rate, dispersions with different phase ratios and consequently, different final polymer concentrations were obtained (**Table 1**).

The morphology and size of these self-assemblies were first studied by TEM. Working under the optimized conditions, homogeneous spherical micelles were obtained (Figure 3b–f) with diameters gradually decreasing (from ≈35 to 20 nm according to the average diameter observed by TEM, Figure S7, Supporting Information) on increasing the percentage of aqueous phase (from **A** to **E** experimental conditions in Table 1). This trend was also observed by DLS (Figure 3g) by which measured D_h values decreased from ≈34 to 23 nm when the percentage of aqueous phase increased. The obtained results are in agreement with the literature,[39,40] where the influence of the organic to aqueous phase ratio on the particle sizes was rationalized in terms of diffusion rate of solvents. The increase of aqueous phase ratio results in decreasing the particle size because the diffusion rate of the water-soluble organic solvent where the polymer is solubilized is also increased. The increase of aqueous/organic phases ratio results in a low polymer concentration and a decrease of viscous forces. Viscous forces oppose the shear stress. Thereby, the decrease of polymer concentration or organic phase content will decrease the length of diffusional pathways into the aqueous phase. Consequently, the rapid migration of THF to the aqueous phase is promoted and the nucleation/growth events are accelerated to yield NPs with smaller size and PdI (Table 1).

2.4. Encapsulation of Naproxen

The potential application of the **PEG-*b*-PDAP** NPs for drug loading (DL) and delivery was tested using naproxen as a model. Naproxen is a nonsteroidal anti-inflammatory drug employed for the treatment of chronic inflammations and autoimmune disorders among other conditions. However, its extended use implies side effects such as gastrointestinal, renal, and cardiovascular complications.[41] In addition, it exhibits low water solubility, which limits its therapeutic effect. The development of new naproxen delivery systems could solve these limitations. Naproxen loaded nanoparticles (**PEG-*b*-PDAP/Npx**) were prepared by microfluidics. Thereby, the drug was dissolved in the polymeric organic phase and dispersions were obtained by microfluidics with a residence time of 48 ms and a 60% of water content (experimental condition **A** according to Table 1). Collected samples were dialyzed against water and then they were filtered to remove nonencapsulated naproxen. Naproxen drug loading and encapsulation efficiency (EE) reached 2.3 ± 0.2 and 3.4 ± 0.4 wt%, respectively (see the Experimental Section, Equations (2) and (3)). The drug loading value is similar than the one reported by Erfani-Moghadam et al.[41] The morphology of **PEG-*b*-PDAP/Npx** NPs was studied by TEM and DLS. Spherical micelles slightly bigger than nonloaded ones, with an average diameter of 37 ± 5 nm, were observed by TEM (Figure S8a,b, Supporting Information) in accordance with the values observed by DLS (Figure S8c, Supporting Information).

The release kinetics of naproxen from **PEG-*b*-PDAP/Npx** NPs was investigated at 25 and 37 °C. As it is observed in **Figure 4**, naproxen was completely released after 148 h at 25 °C. However, a faster release of the encapsulated naproxen was observed at 37 °C (32 h for complete release). These results showed that the increase of temperature boosts the release of the encapsulated naproxen. DLS measurements performed at 25 and 37 °C for these **PEG-*b*-PDAP/Npx** NPs did not show remarkable differences depending on the temperature (Figure S9, Supporting Information).

In order to understand the release kinetics and the transport mechanics involved in the naproxen release, different models were used to fit the experimental data using OriginPro 2021 software. According to the results obtained, the best fitting model to the experimental data was Peppas-Sahlin model,[42] explained by Equation (1), in which M_t and M_∞ are the cumulative drug release at time t and infinite time, respectively; K_1 and K_2 are kinetic constants and m is the diffusional exponent. This model consid-

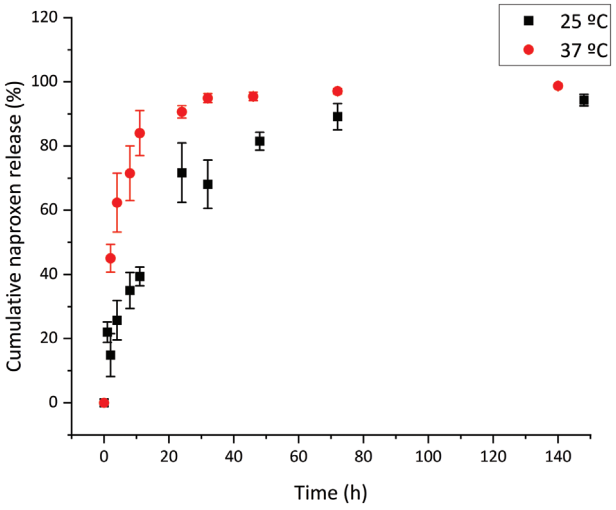

Figure 4. Release profile of naproxen from polymeric nanoparticles at 25 and 37 °C.

ers two competing release mechanisms: Fickian diffusional release, related to molecular diffusion of the drug due to a chemical potential gradient (first term of Equation (1)), and a Case-II relaxational release, related to drug transport caused by hydrophilic polymer chain swelling in water or biological fluids (second term of Equation (1)).

$$\frac{M_t}{M_\infty} = K_1 t^m + K_2 t^{2m} \quad (1)$$

The values obtained by fitting the release data for the diffusional coefficient m (see Table S1 and Figure S10, Supporting Information) were lower than 0.43 for release at 37 °C, so Fickian diffusion was the principal release-controlling mechanism. However, m value obtained for release at 25 °C was higher than 0.43 but lower than 0.85, so this can be described as an anomalous transport case in which, even though Fickian diffusion contribution was predominant, Case-II relaxational contribution significantly influenced on the naproxen release.[42]

2.5. Preparation of Hybrid Pd-Polymeric NPs by Microfluidics

The direct encapsulation of metallic nanomaterials in polymeric NPs is challenging, since the encapsulation control and reproducibility is limited.[12] Our previous findings, where metallic nanomaterials were formed in situ and inside PLGA NPs obtained by a double emulsion process in continuous flow with an excellent control,[43] inspired us to adapt it to this nanoprecipitation approach. Then, as far as we know from the literature, this work is the first one dealing the in situ reduction of Pd precursors inside BC micelles produced by a nanoprecipitation continuous approach. For that purpose, potassium tetrachloropalladate(II) (K_2PdCl_4) was added to the organic phase together with the BC to promote the encapsulation during nanoparticle formation. In order to obtain dispersions with a higher concentration of NPs containing Pd(II), the experimental condition coded as **A**, with a residence time of 48 ms and a water content of 60%, was chosen. The nanoparticle dispersions prepared by microfluidics, which shown a yellowish color due to the presence of Pd(II) (**Figure 5**a), were subjected to a reducing treatment where Pd(II) cations loaded inside **PEG-*b*-PDAP** micelles were reduced to Pd(0). The reduction reaction was carried out by a reductive gas atmosphere where CO gas molecules diffuse through the polymer matrix to promote the electron exchange. For this purpose, polymeric NPs were exposed to a CO atmosphere at 30 °C for 40 min in an attempt to induce the formation of Pd nanosheets according to a method previously reported for hybrid Pd nanosheets-containing exosomes.[23] A color change from orange to dark blue hue was clearly observed (see Figure 5b) that can be attributed to the metal reduction. Then, the dispersion was dialyzed against water. CO molecules serve not only as reducing agent but also as capping agent to promote the anisotropic growth of Pd nanosheets. CO is preferentially adsorbed to basal {111} planes, confining the 2D growth of Pd.[44] Interestingly, this type of Pd nanostructure is featured with a surface plasmon resonance in the NIR range.[25,44] The hybrid NPs, coded as **PEG-*b*-PDAP/Pd**, were studied by TEM and ultrahigh resolution-high angle annular dark field-scanning TEM (UHR–HAADF-STEM). TEM images (Figure 5c) first showed that Pd nanosheets were only observed within the polymeric NPs, inferring that the proposed method to load Pd nanostructures by the in situ reduction approach is highly selective. Interestingly, Pd nanosheets were loaded in all the polymeric NPs. This synthesis procedure was reproduced at least five times, achieving a total control in Pd selective loading in all the polymeric NPs analyzed ($N > 250$). This fact is highly relevant since loading control and reproducibility are the major drawbacks in the production of hybrid nanomaterials when using batch processes. Also, the obtained results evidence that the efficient mixing inside the micromixer with a 48 ms residence time is homogenous enough to achieve an equal loading of Pd(II) precursor in all the nanoparticles produced. Morphology agrees with the formation of nanosheets. Some nanosheets are tilted and enable the cross-section view (Figure 5c). UHR-HAADF-STEM was selected to further study the **PEG-*b*-PDAP/Pd** structure (Figure 5d). Pd nanosheets were selectively localized inside the polymeric NPs and showed variable lengths up to 20 nm and a thickness of 2.0 ± 0.3 nm (Figure 5d). The atomic composition of **PEG-*b*-PDAP/Pd** NPs was studied by energy dispersive X-ray spectroscopy (EDS) and the results also confirm the hybrid nature of these Pd nanosheets-containing polymeric NPs as Pd was clearly detected within these assemblies (Figure S11, Supporting Information). In this way, the encapsulation ability of the polymeric micelles and the possibility of inducing chemical reactions inside of the micelles were consequently demonstrated.

DLS measurements showed that the resulting **PEG-*b*-PDAP/Pd** nanoparticle sizes were slightly larger than that of the corresponding to **PEG-*b*-PDAP** NPs prepared under similar experimental conditions without Pd precursor. Figure 5e displays the shift of the DLS curve as consequence of the encapsulation of the Pd precursor and subsequent reduction to produce the hybrid Pd nanosheet-containing polymeric (**PEG-*b*-PDAP/Pd**) NPs. D_h of the **PEG-*b*-PDAP/Pd** NPs was 36 ± 15 nm and with a PdI = 0.17. The content of Pd determined by inductively coupled plasma optical emission spectroscopy (ICP-OES) (see the Experimental Section, Equation (4)) was 14.7 ± 0.1 wt%.

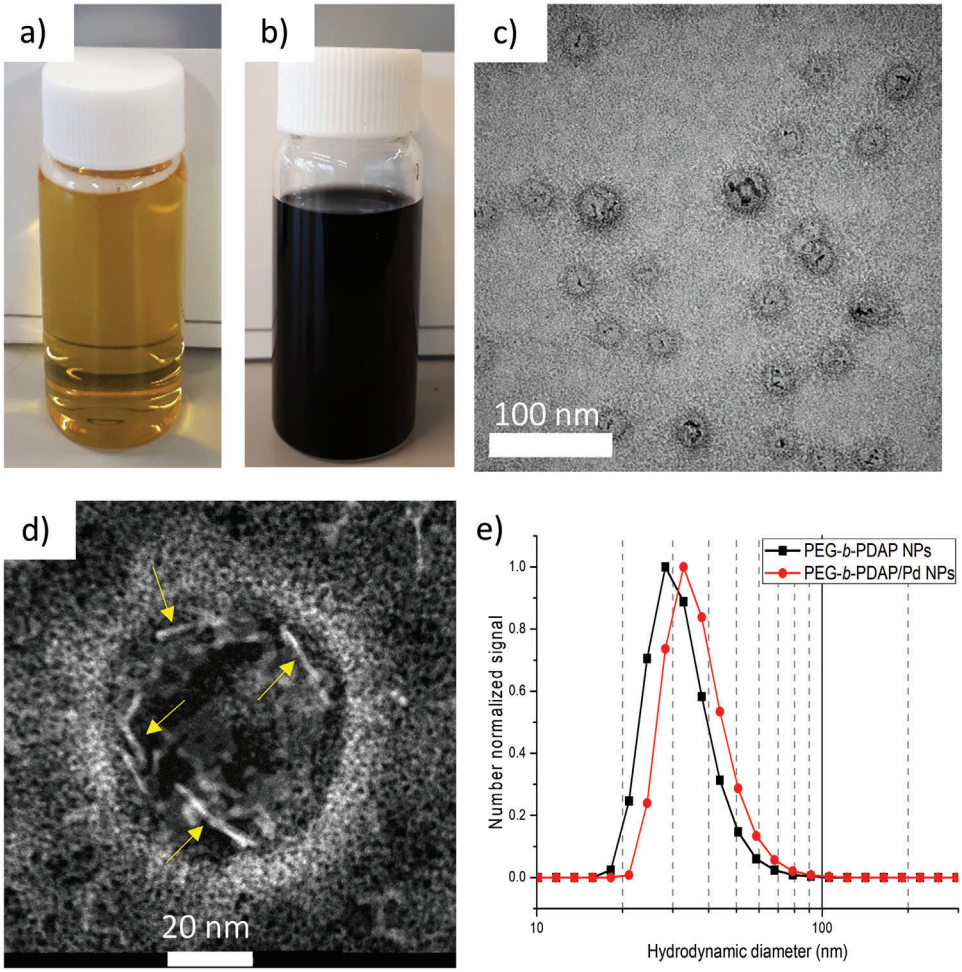

Figure 5. Hybrid Pd-polymeric NPs, **PEG-*b*-PDAP/Pd**, aqueous dispersion a) before and b) after reducing treatment. c) TEM and d) UHR HAADF-STEM images of **PEG-*b*-PDAP/Pd** NPs (yellow arrows indicate Pd nanosheets). e) Number particle size distributions recorded by DLS of **PEG-*b*-PDAP/Pd** and **PEG-*b*-PDAP** NPs.

As it has been mentioned above, light plasmonic absorption in the NIR region and its efficient transduction into heat has been reported for Pd-nanosheets. Consequently, the photoresponse of these **PEG-*b*-PDAP/Pd** NPs (see UV–vis–NIR spectrum in Figure S12, Supporting Information) was studied by monitoring the increase of temperature upon irradiation with an NIR laser (808 nm, 1.5 W cm^{-2}). Thus, a **PEG-*b*-PDAP/Pd** NPs dispersion (adjusted to 0.4 mg mL^{-1} polymer concentration, what was the determined subcytotoxic dose as it is shown below) was first thermostated at 27 °C and then irradiated until reaching a temperature of 45 °C, gained after 1.7 min of irradiation (**Figure 6**a), because at this temperature it has been reported cell death by hyperthermia.[45] To check the resilience of these **PEG-*b*-PDAP/Pd** NPs, the system was first left to cool down to physiological temperature (37 °C, reached 3 min after switching off the NIR source) and then subjected to several on/off NIR irradiation cycles so that the sample was heated to ≈45 °C by NIR irradiation and subsequently cooled to 37 °C by switching the laser off. The photothermal behavior was reproducible after several cycles, which shows the stability of the NPs under these irradiation conditions as well as their potential reusability. This was corroborated by TEM inspection of **PEG-*b*-PDAP/Pd** NPs as after 9 on/off irradiation cycles no significant morphological changes were observed (Figure S13, Supporting Information). The D_h of both **PEG-*b*-PDAP/Pd** and **PEG-*b*-PDAP** NPs were studied by DLS at 25, 37, and 45 °C (Figure 6b,c) and no significant differences were found among them.

2.6. Cell viability, Apoptosis, and Cell Cycle Evaluation

The cytotoxicity was first evaluated in five cell lines (U251MG, mouse mesenchymal stem cells (mMSCs), human macrophages, B16F1 and human dermal fibroblasts). For that purpose, aqueous dispersions of **PEG-*b*-PDAP** and **Pd/PEG-*b*-PDAP** NPs (prepared by microfluidics using experimental conditions **A** in Table 1) were tested in the different cell lines at different nanoparticle concentrations, which were adjusted from 0.025 to 0.4 mg mL^{-1}. Cell viability was estimated by the cell metabolism assay (**Figure 7**a,b). These results showed that cell viability was higher than 70% for both samples and for all the assayed concentrations, although being close to that value for macrophages and fibrob-

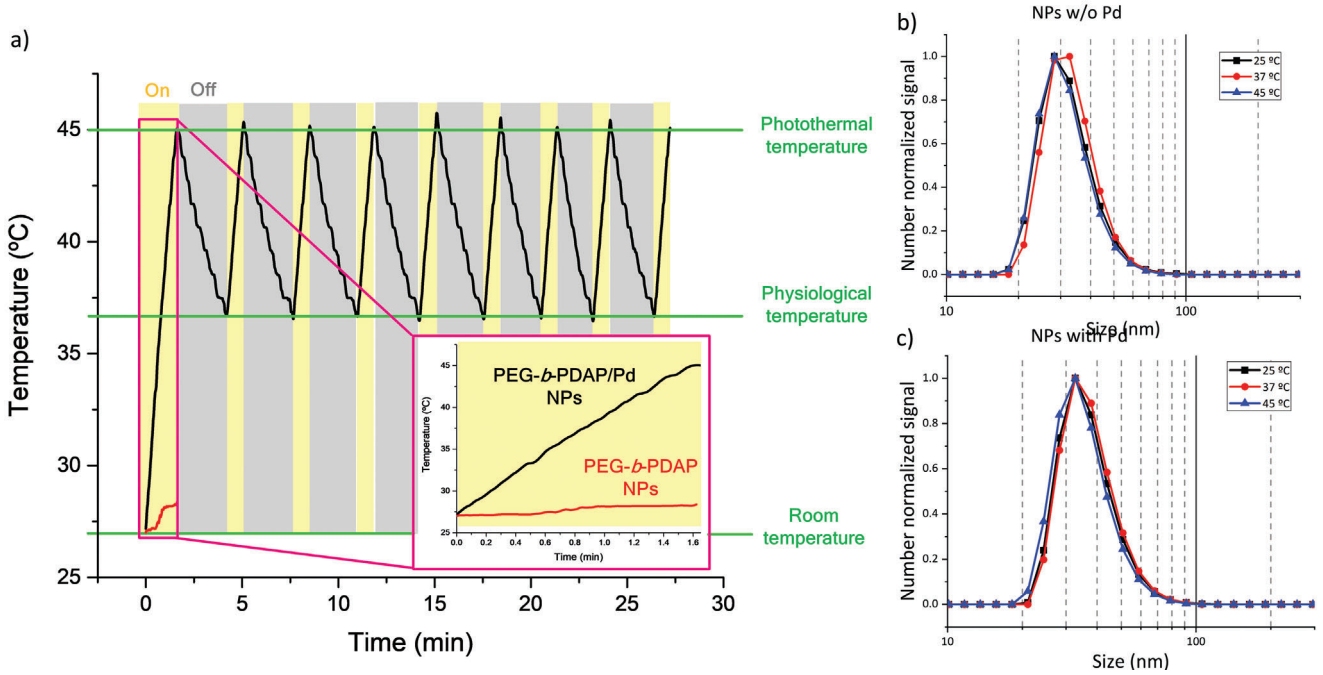

Figure 6. a) Temperature profile of **PEG-*b*-PDAP/Pd** NPs aqueous dispersion (0.4 mg mL^{-1}) over on/off cycles of NIR irradiation (808 nm, 1.5 W cm^{-2}). DLS measurements of b) **PEG-*b*-PDAP** and c) **PEG-*b*-PDAP/Pd** NPs at the different temperatures.

lasts for both samples at 0.4 mg mL^{-1}. Considering these results and the recommendations of the standard ISO 10993-5,[46] the subcytotoxic concentration chosen for further studies was 0.4 mg mL^{-1}, which was the maximum concentration that could be assayed with a viability percentage ≥70% in all cell lines evaluated.

Even though NPs do not show cytotoxicity at the concentration assayed, they could disrupt cell cycle steps and cause DNA damage or apoptosis. Consequently, in order to evaluate the effects of both types of NPs on the cell membrane and nuclei, cell apoptosis and cell cycle studies were performed using flow cytometry. To know the potential cell membrane effects caused by **PEG-*b*-PDAP** and **PEG-*b*-PDAP/Pd** NPs, cell apoptosis studies of both samples were made at the subcytotoxic concentration of 0.4 mg mL^{-1}, and the results obtained are shown in Figure 7c. As it can be seen, no noticeable changes compared to control samples were observed for any cell line, except for macrophages treated with **PEG-*b*-PDAP/Pd** NPs, in which cell viability and necrosis percentages decreased while early and especially late apoptosis percentages increased (≈30%). However, this effect was not observed in the other cell lines tested in which early+late apoptosis did not yield significant changes (<10%). This might be explained as a higher cell uptake of **PEG-*b*-PDAP/Pd** NPs by macrophages. Those results agree with the previous literature as it has been reported that compared to professional phagocytes (e.g., macrophages, monocytes, neutrophils, and dendritic cells) many other cell lines such as fibroblasts show also phagocytic character but at a much lower extent.[47] In this regard, Weissleder et al. showed that out of 12 different cell lines, including tumoral cell lines, the highest nanoparticle uptake occurs into macrophages and the lowest uptake into nondividing parenchymal cells.[48] For mMSCs, it was observed a slight rise in the levels of apoptosis, although for them as well as for the rest of cell lines, viability percentages were similar than control assays ones and all of them were higher than 70%. Therefore, both samples showed appropriate cytocompatibility for biomedical applications according to the recommendations of ISO 10993-5.[46]

Results obtained from cell cycle distribution studies are displayed in Figure 7d. For macrophages and B16F1 cells, not remarkable changes compared to control cells were observed. In the case of mMSCs, a slight increase in G1 and S phases with a concomitant decrease in G2 phase was noticed. An increase of G1 population (<20%), together with a countervailing decrease in S population was observed for U215MG, whereas an increase in S phase (<15%) together with a decrease in G2 phase was observed for fibroblasts. Nonetheless, changes compared to control cells depended on each cell line, but they were not notable.

2.7. Photothermal In Vitro Effects

Photothermal effects of **PEG-*b*-PDAP/Pd** NPs were evaluated on human macrophages and B16F1 cells, using fluorescence microscopy (**Figure 8**). To study this effect, both cell lines were incubated for 24 h with **PEG-*b*-PDAP/Pd** aqueous dispersions, having a concentration adjusted to 0.4 mg mL^{-1}. After removing non-internalized **PEG-*b*-PDAP/Pd** NPs, cells were irradiated for 10 min with 808 nm NIR-laser (1.5 W), and there were not significant temperature changes between irradiated and not irradiated sample wells. Then, samples were studied by fluorescence microscopy after staining live cells with calcein and dead ones with ethidiumbromide. Using this technique, cell death on the irradiated area for both cell lines with internalized **PEG-*b*-PDAP/Pd**

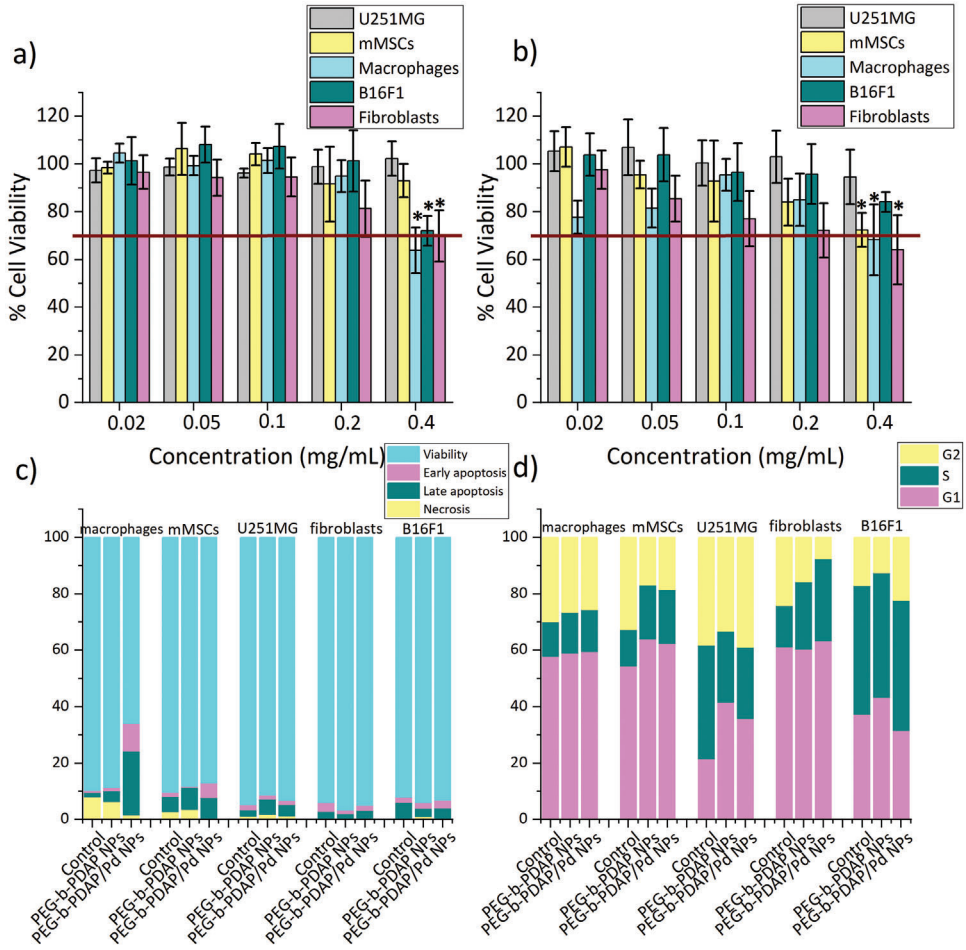

Figure 7. Cell viability in the five cell lines assayed of a) **PEG-*b*-PDAP** and b) **PEG-*b*-PDAP/Pd** NPs prepared by microfluidics (experimental conditions **A**, Table 1; red lines correspond to 70% cell viability, the minimum recommended for considering a subcytotoxic concentration according to ISO-10993).[46] c) Distribution of early and late apoptotic, alive and necrotic cells and d) cell cycle population distribution (percentage of cells, %) after treatment with **PEG-*b*-PDAP** and **PEG-*b*-PDAP/Pd** NPs prepared by microfluidics (experimental conditions **A**, Table 1), with nanoparticle concentration adjusted to 0.4 mg mL^{-1}. Cell viability percentages are expressed as the mean ± SD of five independent experiments showing statistically significant differences between the control sample (not treated cells) and cells treated with **PEG-*b*-PDAP** or **PEG-*b*-PDAP/Pd** NPs ($^*p \leq 0.05$).

NPs was observed (Figure 8). In order to confirm that the cell damage can be associated to the hyperthermia effect induced by NIR irradiation on cells with internalized **PEG-*b*-PDAP/Pd** NPs, control samples treated with **PEG-*b*-PDAP/Pd** NPs but nonirradiated as well as cells nonincubated with **PEG-*b*-PDAP/Pd** nanoparticles and irradiated were also studied (not shown). However, in these cases, cell damage was not observed in both cell lines. As it is observed in Figure 8, cell damage seems to be slightly higher in macrophages than in B16F1 cells, and it might be due to a higher cell uptake of **PEG-*b*-PDAP/Pd** NPs by macrophages being professional scavengers. Regardless, **PEG-*b*-PDAP/Pd** NPs have demonstrated to be a potential agent for photothermal therapy, producing cell death upon internalization and selective NIR irradiation.

3. Conclusion

Preparation of self-assemblies from **PEG-*b*-PDAP** block copolymer has been optimized by microfluidics to obtain homogeneous polymeric NPs in a reproducible and fast manner. This technique has been successfully applied to the preparation of hybrid Pd-polymeric (**PEG-*b*-PDAP/Pd)** NPs as photothermal transductors. For the first time, Pd nanosheets have been prepared by reducing a Pd precursor encapsulated inside of the core of block polymer (**PEG-*b*-PDAP)** micelles during their formation by microfluidics. Pd nanosheets growth in this way does not disrupt **PEG-*b*-PDAP** assembly and avoids the use of highly toxic surfactants. This methodology has been demonstrated to be a reproducible way to get homogeneous Pd loadings inside polymeric micelles. These **PEG-*b*-PDAP/Pd** NPs have not shown cytotoxicity at doses below 0.4 mg mL^{-1}, and they have not disrupted the cell cycle phases and caused DNA damage or apoptosis. Moreover, their photothermal ability was demonstrated in vitro showing cell death in the irradiated area of cell cultures. This fact together with their small size, their ability to be internalized into cells and their high stability, become them in potential materials for photothermal therapy, as it has been evaluated, as well as drug nanocarriers.

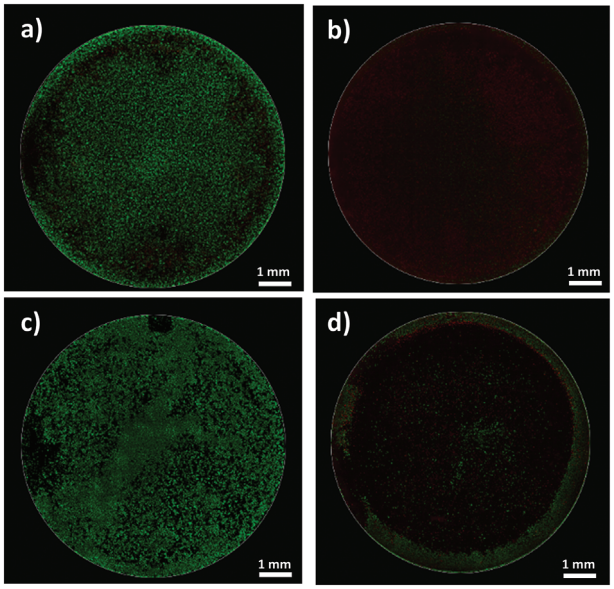

Figure 8. Photothermal effects on macrophages (a and b) and B16F1 cells (c and d). (a) and (c) show cells treated with **PEG-*b*-PDAP/Pd** NPs but not irradiated, while (b) and (d) showed cells treated with **PEG-*b*-PDAP/Pd** NPs and irradiated for 10 min (808 nm, 1.5 W). Samples were observed under fluorescence microscope, showing live cells in green and dead cells in red.

4. Experimental Section

Materials: Macro-CTA poly(ethylene glycol) methyl ether 4-cyano-4-(phenylcarbonothioylthio) pentanoate with a molar mass of 10 000 g mol^{-1} (**PEG-macroCTA**) was purchased from Merck (Merck KGaA, Darmstadt, Germany). Its commercially reported average molar mass was verified by Matrix-assisted laser desorption/ionization-time of flight (MALDI-TOF) mass spectroscopy (M_n = 9685.6 g mol^{-1} was the more intense m/z peak) and ^{1}H NMR (degree of polymerization = 227, M_n = 9999 g mol^{-1}, Figure S1, Supporting Information). Methacrylate monomer **DAP** was synthesized following previously reported procedures.[34] Naproxen sodium was purchased from Merck and converted into its free acid form before encapsulation. Briefly, naproxen sodium (150 mg) was dissolved in Milli-Q water (7 mL) and HCl 0.2 M was added dropwise until approximately pH 3. Naproxen was separated from the solution as a white precipitate that was isolated by filtering, thoroughly washed with water and dried. Finally, the solid was dissolved in dichloromethane (high performance liquid chromatography HPLC grade), filtered through a 0.2 µm polytetrafluoroethylene (PTFE) filter, the solvent removed and the isolated naproxen vacuum dried. Potassium tetrachloropalladate(II) 99.99% was also purchased from Merck and used as received.

Characterization Techniques: Fourier transformed infrared spectroscopy (FTIR) analysis was performed on a Bruker Vertex 70 spectrophotometer having an ATR Golden Gate accessory (Specac). Solution NMR experiments were carried out on Bruker AV-400 spectrometer operating at 400 MHz for ^{1}H. Chemical shifts are given in ppm relative to TMS and the solvent residual peak was used as internal reference. MALDI-TOF mass spectrometry was performed on an Autoflex Bruker mass spectrometer, employing dithranol as matrix. Positive ion electrospray ionization high resolution (ESI HR$^+$) was performed using Bruker Q-TOF-MS in a positive ESI mode. GPC was performed using a Water Alliance 2695 liquid chromatography system with a Waters 2424 evaporative light scattering detector and a Waters 2998 PDA detector, using two columns, PLgel 5 µm MIXED-C and PLgel 3 µm MIXED-E from Agilent (7.5 × 300 mm), and THF (HPLC grade) as eluent (flow 1 mL min^{-1}). Calibration was made with poly(methyl methacrylate) narrow molecular weight standards. UV–vis spectra were recorded on a Varian CaryBio 100 UV–vis spectrophotometer. Fluorescence measurements were performed using a Perkin Elmer LS 50B fluorescence spectrophotometer. DLS measurements were carried out in a Malvern Instrument Nano ZS using a He-Ne laser with a 633 nm wavelength, a detector angle of 173° at 25 °C. The self-assemblies were measured at ≈0.1 mg mL^{-1} concentration. Three measurements of each sample were performed to ensure reproducibility and data of D_h and PdI were calculated from the Gaussian fit of the average experimental number signal using OriginPro2021. TEM analysis was developed in an FEI Tecnai T20 microscope, operating at 200 kV. Aberration corrected scanning TEM (Cs-corrected STEM) images were acquired using an HAADF detector in an FEI XFEG TITAN electron microscope operating at 300 kV equipped with a CETCOR Cs-probe corrector from CEOS. Elemental analysis was carried out with an EDS using an EDAX detector, which allows performing EDS experiments in scanning mode. Samples were prepared placing a droplet of self-assemblies' dispersion on a continuous carbon film-copper grid, and the excess was removed by capillarity using filter paper. Then, samples were stained with uranyl acetate (1% aqueous solution), removing the excess by capillarity using filter paper. The grids were dried overnight under vacuum. TEM size data was reported as the mean ± SD (standard deviation) of 150 measurements histogram. Photothermal experiments were performed using an 808 nm laser diode (model MDL-III-808-2W, Changchun New Industries Optoelectronics Technology Co.). Samples were irradiated using a laser irradiance of 1.5 W cm^{-2} while sample temperature was being monitored.

Synthesis of PEG-b-PDAP: **PEG-*b*-PDAP** was synthesized according to the procedure reported by Concellón et al.[29] **PEG-macroCTA** (0.15 g, 0.015 mmol), monomer **DAP** (0.227 g, 0.60 mmol), and 2,2'-azobisisobutyronitrile (0.36 mg, 0.002 mmol) were dissolved in dried and freshly distilled *N,N*-dimethylformamide (1.5 mL) into a Schlenk flask. Three Ar/vacuum cycles were carried out to deoxygenate the system and the reaction mixture was stirred at 70 °C for 5 h. The reaction was then quenched with liquid nitrogen and the crude precipitated into cold diethyl ether (100 mL). The polymer was isolated by filtering, dried under vacuum, and obtained as a pink powder. Yield: 53%.

^{1}H NMR (400 MHz, $CDCl_3$, δ): 9.05–8.31 (40H), 8.00–7.45 (80H), 4.55–3.97 (109H), 3.89–3.43 (910H), 3.39 (s, 3H), 2.88–2.55 (104H), 2.46–2.24 (54H), 2.04–1.71 (78H), 1.44–0.67 (170H); FTIR (attenuated total reflectance, ATR), ν (cm^{-1}): 3304, 2895, 1732, 1697, 1587, 1520, 1450, 1282, 1244, 1151, 1101; GPC data (Figure S2, Supporting Information): M_n = 15 × 10^3 g mol^{-1}, $Đ$ = 1.04.

Preparation of Polymeric NPs by Nanoprecipitation: Milli-Q water was gradually added to a solution containing 5 mg mL^{-1} of **PEG-*b*-PDAP** in THF (HPLC grade), previously filtered through a 0.2 µm PTFE filter. The self-assembly process was followed by turbidimetry recording the decrease of transmitted light intensity at 650 nm due to aggregation. Once a constant value was reached, the dispersion was dialyzed against a large volume of Milli-Q water, in order to remove THF, employing a Spectra/Por dialysis membrane (molecular weight cut-off, MWCO 1 kDa) (Repligen Europe B.V., Breda, the Netherlands) for 4 d (water was periodically refreshed).

Determination of the CAC: CAC was determined by fluorescence spectroscopy employing Nile Red as a probe, following a previously reported method.[36] First, 100 µL of a Nile Red solution in dicloromethane (6.0 × 10^{-6} M) was added into a series of flasks and then the solvent evaporated. Afterwards, water suspensions of self-assemblies were added to each flask and concentrations adjusted in the range from 1.0 × 10^{-4} to 1.0 mg mL^{-1}. The resulting dispersions were stirred overnight at room temperature to reach equilibrium before fluorescence was measured. The emission spectra of Nile Red were recorded from 560 to 700 nm while exciting at 550 nm. The maximum emission at different concentrations was represented and the CAC calculated as the intersection of two extrapolated lines of the Nile Red emission plot (Figure S5, Supporting Information).

Preparation of Polymeric NPs by Microfluidics: For the preparation of polymeric NPs by microfluidics, **PEG-*b*-PDAP** was dissolved in THF (HPLC grade) to a 5 mg mL^{-1} concentration. After being filtered through a 0.2 µm PTFE filter, this organic solution was fed into an interdigital passive micromixer together with Milli-Q water using two syringe pumps Harvard

Apparatus PHD Ultra CP 4400 (Harvard Apparatus, Holliston, MA, USA), one for each solution. The micromixer employed was a commercial slit interdigital microstructured mixer from Institut für Mikrotechnik Mainz GmbH, Germany interfaced with 0.76 mm internal diameter PTFE tubing. This micromixer, which has an inner volume of 8 µL, was designed for dividing the inlet streams into 15 channels of 40 µm each that were merged at the outlet, achieving instant mixing.[27] Injection flow rates were adjusted to obtain different total flow rates (mixing times) and different values of the water content. Samples were collected after waiting several seconds to micromixer's steady state. Then they were dialyzed against Milli-Q water to remove THF, using a Spectra/Por dialysis membrane (MWCO 1 kDa) for 4 d (water was periodically refreshed).

Naproxen-loaded polymeric NPs (**PEG-b-PDAP/Npx**) were prepared by microfluidics as above described from a solution of naproxen and **PEG-*b*-PDAP** (1:2 wt ratio naproxen/**PEG-*b*-PDAP**) in THF. The final concentration of the polymer was 5 mg mL^{-1}. After dialysis, **PEG-*b*-PDAP/Npx** NPs dispersion was filtered through a 0.2 µm CA filter to remove nonencapsulated naproxen. The **PEG-*b*-PDAP/Npx** concentration was determined by gravimetry of an evaporated given volume (average of at least three samples). The loaded naproxen was determined by HPLC, by previous lyophilization of an aliquot of the sample (600 µL) and by its redissolution in a mixture of water/methanol (1:1). HPLC measurements were performed using a Waters 600 controller pump system, a Waters 2998 photodiode array detector and a Waters Spherisorb C8 column (250 mm × 4.6 mm, 5 µm particle size). The mobile phase was 1.8×10^{-3} M phosphoric acid (pH 2.8)/acetonitrile (1:1, v/v) at a flow rate of 1 mL min^{-1} and the injection volume was 10 µL. Detection was carried out at 272 nm. Quantification of naproxen was performed from peak area measurements in relation to those of standards chromatographed under the same conditions. DL and EE were calculated by Equations (2) and (3):

$$\text{DL (wt\%)} = \frac{\text{Mass of naproxen in nanoparticles (mg)}}{\text{Mass of polymeric nanoparticles (mg)}} \times 100 \quad (2)$$

$$\text{EE (wt\%)} = \frac{\text{Mass of naproxen in nanoparticles (mg)}}{\text{Naproxen fed in the system (mg)}} \times 100 \quad (3)$$

Hybrid Pd-polymeric NPs (**PEG-*b*-PDAP/Pd**) were prepared by microfluidics as described for polymeric NPs with only the organic solution being modified as follows: To promote the Pd precursor internalization into the formed micelles, the organic solution was prepared by adding a potassium tetrachloropalladate(II) (K_2PdCl_4) solution in dimethyl sulfoxide DMSO (HPLC grade) to the BC solution in THF. The final concentration of the polymer was 5 mg mL^{-1} in a THF-DMSO (9:1) solution with a ratio 1:2 w/w K_2PdCl_4/**PEG-*b*-PDAP**. Samples collected at the outlet of the micromixer were loaded into a stainless steel Teflon lined autoclave and subjected to a reducing treatment under CO atmosphere (6 bar) at 30 °C for 40 min to reduce the precursor into Pd nanosheets.[23] Then, they were dialyzed against Milli-Q water.

The amount of Pd in the final nanoparticles was determined by ICP-OES spectroscopy. Samples were previously digested using aqua regia and the amount of Pd was calculated according to Equation (4)

$$\text{Pd content (wt\%)} = \frac{\text{Mass of Pd (mg)}}{\text{Mass of hybrid nanoparticles (mg)}} \times 100 \quad (4)$$

In Vitro Release of Naproxen from Polymeric NPs: Naproxen release studies in phosphate buffered saline (PBS) solution were performed at 25 and 37 °C. An aliquot of the naproxen-loaded polymeric NPs dispersion (100 µL) was loaded into a dialysis cup (Slide-A-Lyzer MINI Dialysis Device, 2K MWCO, 0.1 mL; ThermoFisher Scientific) and dialyzed against PBS (1.6 mL) at the selected temperature. At a given time, the sample was removed from the dialysis cup, lyophilized, and redissolved in a mixture of water/methanol (1:1). Naproxen content was determined by HPLC. Samples were measured at different dialysis times in triplicate.

Cell Culture: The cytocompatibility of the polymeric and hybrid NPs was assessed at different levels regarding cell metabolism, cell membrane (induction of apoptosis and/or necrosis), and cell nucleus (distribution of cell cycle phases). These studies were performed by using THP1 human macrophages (obtained from the American Type Culture Collection, US), human dermal fibroblasts (purchased from Lonza, Belgium), mMSCs, human glioblastoma cells (U251MG), and mouse melanoma cells (B16F1) (kindly gifted by Dr. Pilar Martín-Duque). Macrophages were obtained by the in vitro differentiation of monocytes for 72 h through the addition of 1×10^{-6} M phorbol 12-mystirate 13-acetate (Sigma-Aldrich, US) to the cell culture medium which was composed of RPMI 1640 (w/stable Glutamine; Biowest, France), 10% fetal bovine serum (FBS; Gibco, UK), 1% HEPES (Lonza, Belgium), 0.1% 2-mercaptoethanol (50×10^{-3} M) (Gibco, UK), 1% nonessential amino acids, 1% sodium pyruvate (100×10^{-3} M), and 1% penicillin-streptomycin-amphotericin B (Biowest, France). Fibroblasts, U251MG, and B16F1 cells were grown in Dubbelco's Modifed Eagle's Medium, DMEM, high glucose (DMEM w/stable Glutamine; Biowest, France) supplemented with 10% FBS (Gibco, UK) and 1% penicillim-streptomycin-amphotericin B (Biowest, France). mMSCs were cultured in DMEM-F12 (Biowest, France) containing 1% glutamine (Biowest, France), 10% FBS (Gibco, UK), and 1% penicillim-streptomycin-amphotericin B (Biowest, France). All cell types were grown at 37 °C and 5% CO_2, except for mMSCs which were cultured in hypoxia (3% O_2).

Cytotoxicity Assays: The effects of polymeric and hybrid NPs in cell metabolism were determined by Blue Cell Viability assay (Abnova, Taiwan), which is based on the reduction of a dye to a fluorescent compound mediated by metabolic active cells. For that purpose, cells were incubated with nanoparticles (0.01–0.4 mg mL^{-1}) for 24 h. Then, the reagent was added (10%) and incubated for 4 h. After that, fluorescence was read at 535/590 nm (ex/em) in a Multimode Synergy HT Microplate Reader (Biotek, US). Cell viability was determined by the interpolation of the emission data obtained from the treated samples and the control ones, which were assigned with a 100% viability. Samples without the cells were also tested to evaluate a potential nanoparticle interference with the methodology.

Evaluation of Early and Late Cell Apoptosis and/or Necrosis: The effects of polymeric and hybrid NPs on cell membrane were determined by a quantitative analysis of cell apoptosis and necrosis by flow cytometry. Cells were incubated with the different samples at the subcytotoxic concentration obtained from the Blue Cell Viability assay for 24 h. Then, cells were harvested in PBS and double stained with annexin V-FITC (fluorescein isothiocyanate) and propidium iodide. Briefly, cell suspensions were stained with annexin V-FITC, treated with a solution composed of annexin V-FITC, propidium iodide and annexin V binding buffer, to be finally incubated with the binding buffer for 15 min before the analysis of the samples in a FACSARIA BD equipment, using the FACSARIA BD software (Cell Separation and Cytometry Unit, CIBA, IIS Aragon, Spain) to calculate the percentages of alive, apoptotic and necrotic cells. Control samples were also evaluated in order to compare the basal status of cells to that obtained after nanoparticles treatment, and samples without the cells were also tested to evaluate a potential nanoparticle interference with the methodology.

Study of Cell Cycle: The effects of polymeric and hybrid NPs on cell cycle and DNA were determined by analyzing the distribution of cell cycle phases by flow cytometry. As described above, cells were incubated with the different samples at the subcytotoxic concentration for 24 h and then, they were collected in PBS and fixed in 70% ice-cold ethanol. Then, samples were washed (2% BSA in PBS), centrifuged (300 g, 5 min), and the pellet were stained with the PI/RNASE Solution (Immunostep, Spain). After incubation for 15 min, samples were analyzed in a FACSARRAY BD equipment with the MODIFIT 3.0 Verity software. Control samples were also evaluated in order to compare the basal status of cells to that obtained after nanoparticle treatment and samples without the cells were also tested to evaluate a potential nanoparticle interference with the methodology.

Photothermal In Vitro Effects: Photothermally induced cell death mediated by hybrid Pd-polymeric NPs upon NIR light irradiation was evaluated. For that purpose, human macrophages and B16F1 cells were seeded on 24-well plates at cell densities of 500 000 and 40 000 cells per well, respectively. Then cells were treated with **PEG-*b*-PDAP/Pd** NPs dispersed with growth medium to reach a concentration of 0.4 mg mL^{-1} (subcytotoxic concentration obtained from the blue cell viability assay). After incubation for 24 h, cells were washed to remove noninternalized nanoparticles. Cells

were irradiated with an NIR laser (808 nm; 10 min at 1.5 W). Changes in cell well temperature were also monitored. Cell damage was evaluated by fluorescence microscopy just after irradiation by using the LIVE/DEAD viability/cytotoxicity kit (Thermo-Fisher Scientific, USA) following the manufacturer instructions. Briefly, a solution containing 2×10^{-6} M calcein AM and 4×10^{-6} M ethidium homodimer-1 was added. After incubation at room temperature (30 min), cells were visualized under an inverted fluorescence microscope Olympus IX81 through the composition of 144 fields on each well acquired at 5X magnification to obtain a mosaic of each well. Control samples (treated and not irradiated, not treated and irradiated, not treated and not irradiated) were also assayed to evaluate the basal status of cells.

Statistical Analyses: Data are reported as the mean ± SD. Normal distribution of the variables was analyzed by the Shapiro-Wilk test followed by the U-Mann–Whitney, ANOVA, or Student *t*-test (StataSE 12 statistical software, StataCorp LP, USA). Statistically significant differences were considered when $p \leq 0.05$.

Supporting Information

Supporting Information is available from the Wiley Online Library or from the author.

Acknowledgements

This work was supported by the "Ministerio de Economía y Competitividad, Programa Excelencia" (MINECO)-FEDER, Spain, under the project grant number MAT2017-84838-P (L.O. and M.P.) and by "Ministerio de Ciencia, Innovación y Universidades, Programa Retos Investigación," grant number: RTI2018-099019-A-I00 (V.S.), "Fondo Social Europeo and Gobierno de Aragón"-"Fondo Europeo de Desarrollo Regional", FEDER (E47_17R, FEDER 2014–2020 "Construyendo Europa desde Aragón"). M.A. acknowledges Gobierno de Aragón and Fondo Social Europeo for her Ph.D. grant. G.M. is also grateful for the support from the Miguel Servet Program (MS19/00092; Instituto de Salud Carlos III). Authors acknowledge the "Centro de Química y Materiales de Aragón (CEQMA)" for the NMR facilities and the use of Electron Microscopy facilities of the "Laboratorio de Microscopías Avanzadas (LMA)." Authors additionally would like to acknowledge the use of "Servicio General de Apoyo a la Investigación-SAI," Universidad de Zaragoza for ICP-OES measurements.

Conflict of Interest

The authors declare no conflict of interest.

Data Availability Statement

The data that support the findings of this study are available in the supplementary material of this article.

Keywords

block copolymer micelles, drug delivery, microfluidics, Pd nanosheets, photothermal therapy

Received: December 28, 2021
Revised: February 10, 2022
Published online: March 18, 2022

[1] G. A. Ozin, A. Arsenault, L. Cademartiri, *Nanochemistry: A Chemical Approach to Nanomaterials*, The Royal Society of Chemistry, Cambridge **2006**.
[2] M. Elsabahy, K. L. Wooley, *Chem. Soc. Rev.* **2012**, *41*, 2545.
[3] H. Cabral, K. Miyata, K. Osada, K. Kataoka, *Chem. Rev.* **2018**, *118*, 6844.
[4] A. Y. Rwei, W. Wang, D. S. Kohane, *Nano Today* **2015**, *10*, 451.
[5] S. Wu, H.-J. Butt, *Adv. Mater.* **2016**, *28*, 1208.
[6] S. Förster, M. Antonietti, *Adv. Mater.* **1998**, *10*, 195.
[7] M. Antonietti, E. Wenz, L. Bronstein, M. Seregina, *Adv. Mater.* **1995**, *7*, 1000.
[8] S. Papp, L. Korosi, B. Gool, T. Dederichs, P. Mela, M. Moller, I. Dekany, *J. Therm. Anal. Calorim.* **2010**, *101*, 865.
[9] A. Balanta, C. Godard, C. Claver, *Chem. Soc. Rev.* **2011**, *40*, 4973.
[10] H. Park, J. Yang, J. Lee, S. Haam, I.-H. Choi, K.-H. Yoo, *ACS Nano* **2009**, *3*, 2919.
[11] Z. Zhang, J. Wang, X. Nie, T. Wen, Y. Ji, X. Wu, Y. Zhao, C. Chen, *J. Am. Chem. Soc.* **2014**, *136*, 7317.
[12] E. Luque-Michel, A. Larrea, C. Lahuerta, V. Sebastián, E. Imbuluzqueta, M. Arruebo, M. J. Blanco-Prieto, J. Santamaría, *Nanoscale* **2016**, *8*, 6495.
[13] R. R. Arvizo, S. Bhattacharyya, R. A. Kudgus, K. Giri, R. Bhattacharya, P. Mukherjee, *Chem. Soc. Rev.* **2012**, *41*, 2943.
[14] A. Dumas, P. Couvreur, *Chem. Sci.* **2015**, *6*, 2153.
[15] X. Huang, S. Tang, X. Mu, Y. Dai, G. Chen, Z. Zhou, F. Ruan, Z. Yang, N. Zheng, *Nat. Nanotechnol.* **2011**, *6*, 28.
[16] S. Tang, X. Huang, N. Zheng, *Chem. Commun.* **2011**, *47*, 3948.
[17] W. Fang, J. Yang, J. Gong, N. Zheng, *Adv. Funct. Mater.* **2012**, *22*, 842.
[18] W. Fang, S. Tang, P. Liu, X. Fang, J. Gong, N. Zheng, *Small* **2012**, *8*, 3816.
[19] S. Tang, M. Chen, N. Zheng, *Small* **2014**, *10*, 3139.
[20] M. Chen, S. Chen, C. He, S. Mo, X. Wang, G. Liu, N. Zheng, *Nano Res.* **2017**, *10*, 1234.
[21] W. Cai, H. Gao, C. Chu, X. Wang, J. Wang, P. Zhang, G. Lin, W. Li, G. Liu, X. Chen, *ACS Appl. Mater. Interfaces* **2017**, *9*, 2040.
[22] J. Ming, J. Zhang, Y. Shi, W. Yang, J. Li, D. Sun, S. Xiang, X. Chen, L. Chen, N. Zheng, *Nanoscale* **2020**, *12*, 3916.
[23] M. Sancho-Albero, B. Rubio-Ruiz, A. M. Pérez-López, V. Sebastián, P. Martín-Duque, M. Arruebo, J. Santamaría, A. Unciti-Broceta, *Nat. Catal.* **2019**, *2*, 864.
[24] V. Sebastián, M. Sancho-Albero, M. Arruebo, A. M. Pérez-López, B. Rubio-Ruiz, P. Martin-Duque, A. Unciti-Broceta, J. Santamaría, *Nat. Protoc.* **2021**, *16*, 131.
[25] A. M. Pérez-López, B. Rubio-Ruiz, T. Valero, R. Contreras-Montoya, L. Álvarez De Cienfuegos, V. Sebastián, J. Santamaría, A. Unciti-Broceta, *J. Med. Chem.* **2020**, *63*, 9650.
[26] V. Sebastián, M. Arruebo, J. Santamaría, *Small* **2014**, *10*, 835.
[27] I. Ortiz De Solorzano, L. Usón, A. Larrea, M. Miana, V. Sebastián, M. Arruebo, *Int. J. Nanomed.* **2016**, *11*, 3397.
[28] C. Yus, S. Irusta, V. Sebastián, M. Arruebo, *Mol. Pharmaceutics* **2020**, *17*, 3314.
[29] A. Concellón, R. Clavería-Gimeno, A. Velázquez-Campoy, O. Abian, M. Piñol, L. Oriol, *RSC Adv.* **2016**, *6*, 24066.
[30] A. Concellón, E. Blasco, A. Martínez-Felipe, J. C. Martínez, I. Šics, T. A. Ezquerra, A. Nogales, M. Piñol, L. Oriol, *Macromolecules* **2016**, *49*, 7825.
[31] S. Marre, K. F. Jensen, *Chem. Soc. Rev.* **2010**, *39*, 1183.
[32] V. Sebastián, S. A. Khan, A. A. Kulkarni, *J. Flow Chem.* **2017**, *7*, 96.
[33] S. García-Salinas, E. Himawan, G. Mendoza, M. Arruebo, V. Sebastián, *ACS Appl. Mater. Interfaces* **2018**, *10*, 19197.
[34] A. Concellón, E. Blasco, M. Piñol, L. Oriol, I. Díez, C. Berges, C. Sánchez-Somolinos, R. Alcalá, *J. Polym. Sci., Part A: Polym. Chem.* **2014**, *52*, 3173.
[35] A. Choucair, C. Lavigueur, A. Eisenberg, *Langmuir* **2004**, *20*, 3894.
[36] E. Blasco, J. del Barrio, C. Sánchez-Somolinos, M. Piñol, L. Oriol, *Polym. Chem.* **2013**, *4*, 2246.
[37] E. A. Rainbolt, K. E. Washington, M. C. Biewer, M. C. Stefan, *Polym. Chem.* **2015**, *6*, 2369.

[38] A. Albisa, E. Piacentini, V. Sebastián, M. Arruebo, J. Santamaría, L. Giorno, *Pharm. Res.* **2017**, *34*, 1296.
[39] A. Budhian, S. J. Siegel, K. I. Winey, *Int. J. Pharm.* **2007**, *336*, 367.
[40] S. Das, P. K. Suresh, R. Desmukh, *Nanomed. Nanotechnol. Biol. Med.* **2010**, *6*, 318.
[41] V. Erfani-Moghadam, M. Aghaei, A. Soltani, N. Abdolahi, A. Ravaghi, M. Cordani, S. Shirvani, S. M. Rad, H. Balakheyli, *J. Mol. Struct.* **2020**, *1211*, 127867.
[42] N. A. Peppas, J. J. Sahlin, *Int. J. Pharm.* **1989**, *57*, 169.
[43] A. Larrea, A. Clemente, E. Luque-Michel, V. Sebastián, *Chem. Eng. J.* **2017**, *316*, 663.
[44] V. Sebastián, C. D. Smith, K. F. Jensen, *Nanoscale* **2016**, *8*, 7534.
[45] A. Shahidian, M. Ghassemi, J. Mohammadi, M. Hashemi, in *Bio-Engineering Approaches to Cancer Diagnosis and Treatment*, Elsevier, New York **2020**, pp. 157–179.
[46] ISO. ISO 10993-5: 2009 Biological Evaluation of Medical Devices-Part 5: Tests for in Vitro Cytotoxicity; ISO: Phoenix, AZ, USA, **2009**, *2007*, pp. 1-11.
[47] S. Behzadi, V. Serpooshan, W. Tao, M. A. Hamaly, M. Y. Alkawareek, E. C. Dreaden, D. Brown, A. M. Alkilany, O. C. Farokhzad, M. Mahmoudi, *Chem. Soc. Rev.* **2017**, *46*, 4218.
[48] R. Weissleder, M. Nahrendorf, M. J. Pittet, *Nat. Mater.* **2014**, *13*, 125.